PAPER • **OPEN ACCESS**

Development and evaluation of dose calculation algorithm with a combination of Monte Carlo and point-kernel methods for boron neutron capture therapy

To cite this article: Mai Nojiri *et al* 2023 *Biomed. Phys. Eng. Express* **9** 035025

Biomedical Physics & Engineering Express

PAPER

Development and evaluation of dose calculation algorithm with a combination of Monte Carlo and point-kernel methods for boron neutron capture therapy

Mai Nojiri[1], Takushi Takata[2], Naonori Hu[2,3], Yoshinori Sakurai[2], Minoru Suzuki[2] and Hiroki Tanaka[2]

[1] Department of Nuclear Engineering, Graduate School of Engineering, Kyoto University, Kyoutodaigaku-Katsura, Kyoto, Japan
[2] Institute for Integrated Radiation and Nuclear Science, Kyoto University, Kumatori-cho, Osaka, Japan
[3] Kansai BNCT Medical Center, Osaka Medical and Pharmaceutical University, Takatsuki, Japan

E-mail: takata.takushi.6x@kyoto-u.ac.jp

OPEN ACCESS

RECEIVED
14 December 2022

REVISED
9 March 2023

ACCEPTED FOR PUBLICATION
10 March 2023

PUBLISHED
6 April 2023

Keywords: boron neutron capture therapy, treatment planning, dose calculation algorithm, Monte Carlo method, point-kernel

Abstract

We developed a 'hybrid algorithm' that combines the Monte Carlo (MC) and point-kernel methods for fast dose calculation in boron neutron capture therapy. The objectives of this study were to experimentally verify the hybrid algorithm and to verify the calculation accuracy and time of a 'complementary approach' adopting both the hybrid algorithm and the full-energy MC method. In the latter verification, the results were compared with those obtained using the full-energy MC method alone. In the hybrid algorithm, the moderation process of neutrons is simulated using only the MC method, and the thermalization process is modeled as a kernel. The thermal neutron fluxes calculated using only this algorithm were compared with those measured in a cubic phantom. In addition, a complementary approach was used for dose calculation in a geometry simulating the head region, and its computation time and accuracy were verified. The experimental verification indicated that the thermal neutron fluxes calculated using only the hybrid algorithm reproduced the measured values at depths exceeding a few centimeters, whereas they overestimated those at shallower depths. Compared with the calculation using only the full-energy MC method, the complementary approach reduced the computation time by approximately half, maintaining nearly same accuracy. When focusing on the calculation only using the hybrid algorithm only for the boron dose attributed to the reaction of thermal neutrons, the computation time was expected to reduce by 95% compared with the calculation using only the full-energy MC method. In conclusion, modeling the thermalization process as a kernel was effective for reducing the computation time.

1. Introduction

Boron neutron capture therapy (BNCT) is a radiation therapy based on a nuclear reaction between a boron-10 nucleus and a thermal neutron (Locher, 1936) [1]. The two ionizing particles (an alpha particle and a lithium-7 nucleus) produced by the reaction have high linear energy transfer; therefore, they can effectively kill cells. The ranges of the produced alpha particles and lithium-7 nuclei are 9 and 4 μm, respectively, which are comparable to the size of a human cell. Therefore, BNCT can selectively kill tumor cells and ensure minimal damage to normal cells, by accumulating a boron drug at the target site before neutron irradiation, and it is considered an effective treatment for intractable cancers (Barth *et al* 2012) [2]. Furthermore, in contemporary BNCT, an epithermal neutron beam with higher energy than a thermal neutron is used for treating deeply located tumors, utilizing the thermalization of neutrons in the body of a patient (Fairchild *et al* 1965) [3]. Accelerator-based neutron sources are preferred over reactor-based ones (Suzuki, 2020) [4]. Recently, cyclotron-based neutron sources have been developed (Tanaka *et al* 2009, Kato *et al* 2020) [5, 6]. In Japan, clinical treatments using accelerator-based neutron sources have been provided since 2020 for unresectable, locally advanced, and recurrent head and neck carcinomas (Kanno *et al* 2021) [7].

Considering the increasing number of patients, treatment planning efficiency has become increasingly important. The Monte Carlo (MC) method has been conventionally used for dose calculation in BNCT treatment planning, because of its high calculation accuracy. Several MC-based treatment planning systems have been developed for BNCT, such as the NeuCure Dose Engine (Sumitomo Heavy Industries, Ltd), which was commercialized as a medical device, and the Tsukuba plan developed by Kumada *et al* [8–10]. The NeuCure Dose Engine and Tsukuba plan allow accurate calculation of dose distribution because they include the Particle and Heavy Ion Transport code System (PHITS), which is an MC code system developed by Sato *et al* [11]. However, in the MC calculation, the particles are tracked until they come to rest. Therefore, high-accuracy MC calculation of the dose distribution requires considerable time, and dose calculation using the MC method can be a bottleneck in the treatment planning process in BNCT, hindering optimization of the irradiation conditions. Hence, a dose calculation algorithm faster than the conventionally used MC method is required, and the realization of such an algorithm can help quickly treat a large number of patients.

Studies on dose calculation algorithms have been conducted using diffusion equations (Takada *et al* 2016, Albertson *et al* 2001) [12, 13]. Takada *et al* divided the continuous neutron energy into eight energy groups used for neutron beam calculations and calculated the spatial distribution of neutrons by solving a fixed-source neutron diffusion equation. The time required for a calculation using this method is shorter than the MC method. However, the calculation accuracy of the method is low—particularly for the fast neutron flux distribution [12]. This is due to the limitations of simplified equations for neutron transport simulations.

Therefore, we developed an algorithm that combines the MC and kernel-based methods (hereinafter called the 'hybrid algorithm') for fast dose calculation with acceptable accuracy. In this algorithm, calculations are performed for two processes of neutrons that have entered a body. The first is the moderation process, in which the energy of the incident neutrons is reduced by collisions with the atomic nuclei in the body. The second is the thermalization process, in which the moderated neutrons reach thermal equilibrium with the atomic nuclei in the body. The former is calculated using the MC method, and the latter is modeled as a kernel in advance, as in the superposition method (Anhesjö *et al* 1987) [14]. In the MC calculation for the moderation process, the tracking of a neutron is terminated when its energy reaches the lower limit to shift to the thermalization process. This reduces the time needed to derive the dose components arising from the interaction of the thermal neutrons with the atomic nuclei of the body. However, this hybrid algorithm has a low calculation accuracy [15]. The currently adopted kernel is calculated in a homogeneous geometry with an infinite volume, and the inhomogeneity of the density of the materials is not considered in kernel modeling. Therefore, calculations using this kernel cannot represent the leakage of thermal neutrons to the surrounding air (outside the body), resulting in the overestimation of the thermal neutron fluxes near the beam incident surface of the body.

Utilizing the result calculated using the full-energy MC method only for the shallow part from 0 to a few centimeters is considered advantageous for complementing the low accuracy of the hybrid algorithm in the shallow region. In the 'full-energy' MC calculation, the MC method is adopted for the calculation of both moderation and thermalization processes, as a conventionally used calculation. The statistical uncertainty associated with the MC calculation can be easily reduced in the shallow region. Therefore, if the result obtained via the full-energy MC calculation is used only for the shallow region, results with sufficiently low statistical uncertainty can be obtained within a shorter time than the calculation adopting the full-energy MC method for the entire region. In addition, the advantage of the hybrid algorithm—the high calculation speed—is not completely removed.

In this study, we propose the hybrid algorithm as the first step in the development of fast dose calculation algorithm and evaluate the calculation accuracy. In addition, we evaluate the calculation accuracy and time of the complementary approach.

2. Materials and methods

The calculation accuracy of the hybrid algorithm was evaluated by comparing the calculated thermal neutron fluxes with the values obtained in an experiment using a cubic phantom. The evaluation of the thermal neutron flux is crucial in BNCT. This is because thermal neutron flux is proportional to the boron and nitrogen doses, which are related to the nuclear reaction of thermal neutrons with boron and nitrogen nuclei, respectively. The boron doses are dominant in BNCT.

Subsequently, we evaluated the calculation accuracy and time of the complementary approach. The complementary calculation was performed under conditions similar to those of clinical treatment. The calculations included fast neutron and gamma-ray doses, in addition to boron and nitrogen doses. The results obtained via the complementary approach were compared with those obtained by adopting the full-energy MC method for the entire region.

In these evaluations, three types of dose calculations were performed: calculations adopting the full-energy MC method for an entire region, calculations adopting the hybrid algorithm for the entire region, and calculations adopting the complementary approach. Hereinafter, these are referred to as the 'entire-full-MC', 'entire-hybrid', and 'complementary' calculations, respectively. In the 'complementary' approach, the entire region was

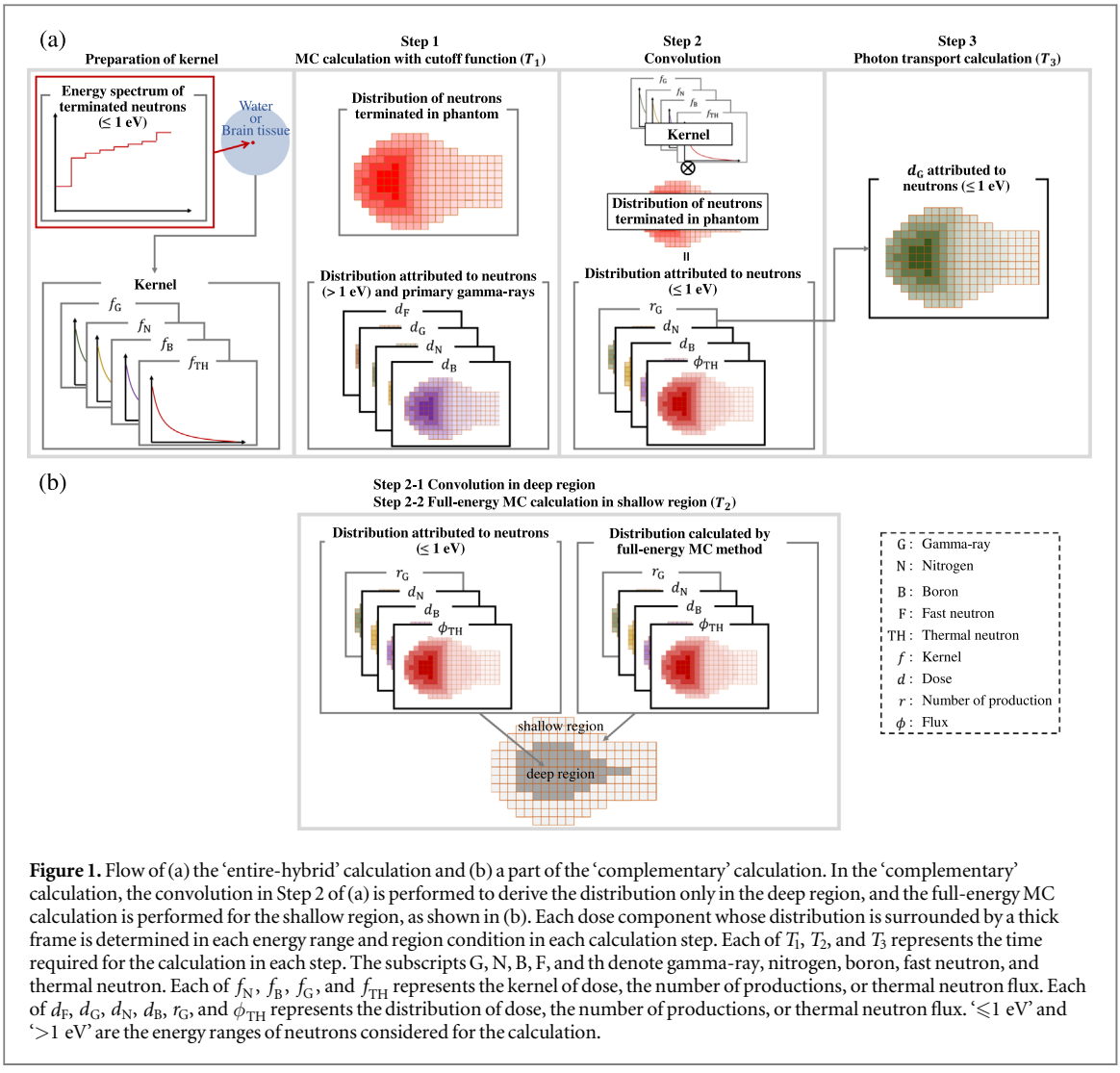

Figure 1. Flow of (a) the 'entire-hybrid' calculation and (b) a part of the 'complementary' calculation. In the 'complementary' calculation, the convolution in Step 2 of (a) is performed to derive the distribution only in the deep region, and the full-energy MC calculation is performed for the shallow region, as shown in (b). Each dose component whose distribution is surrounded by a thick frame is determined in each energy range and region condition in each calculation step. Each of T_1, T_2, and T_3 represents the time required for the calculation in each step. The subscripts G, N, B, F, and th denote gamma-ray, nitrogen, boron, fast neutron, and thermal neutron. Each of f_N, f_B, f_G, and f_{TH} represents the kernel of dose, the number of productions, or thermal neutron flux. Each of d_F, d_G, d_N, d_B, r_G, and ϕ_{TH} represents the distribution of dose, the number of productions, or thermal neutron flux. '$\leqslant$1 eV' and '$>$1 eV' are the energy ranges of neutrons considered for the calculation.

divided into two regions at the separation surface, which were located at a few centimeters away from the body surface of the head phantom, and the full-energy MC method and hybrid algorithm were adopted for the shallow and deep regions, respectively. The 'entire-full-MC' and 'entire-hybrid' calculations using a cubic phantom were experimentally verified with regard to the calculation accuracy; 'entire-full-MC' and 'complementary' calculations using a geometry simulating a head region were verified with regard to the computation time and calculation accuracy.

The MC calculation was performed using PHITS ver. 3.24 (Sato *et al* 2018) [11]. For the PHITS calculations, shared-memory parallel computing was conducted using a multi-core central processing unit (i9-10900, Intel Corporation, 10 cores).

2.1. Calculation using hybrid algorithm

2.1.1. Flow of calculation using hybrid algorithm

In the calculation using the hybrid algorithm, the moderation process of the neutrons is calculated using the MC method with a cut-off function implemented in PHITS, and the thermalization process is modeled as a kernel in advance. In the MC calculation with a cut-off function, the particle transport is stopped below the preset cutoff energy. In this study, the energy where the neutrons need to reach the lower limit to switch from the moderation process to the thermalization process (the cut-off energy) was set as 1 eV.

As shown in figure 1(a), the calculation using the hybrid algorithm was performed as follows. First, the kernels of the thermal neutron flux and dosimetric quantities related to the thermal neutrons, including the boron dose, nitrogen dose, and number of secondary gamma-rays produced, were precalculated. Here, the boron and nitrogen doses were attributed to ^{10}B(n, α)^{7}Li and ^{14}N(n, p)^{14}C, respectively. In addition, the reactions of ^{1}H(n, γ)^{2}H, ^{10}B(n, $\alpha\gamma$)^{7}Li, ^{40}Ca(n, γ)^{41}Ca, and ^{31}P(n, γ)^{32}P were considered for the calculation of the number of secondary gamma-rays. In the calculation, the neutron source was set as a point source with an energy spectrum of neutrons terminated below 1 eV. The distributions of the above quantities generated by the source were obtained via an MC calculation in a homogeneous geometry with a sufficiently large volume. Therefore, the kernel used in this study

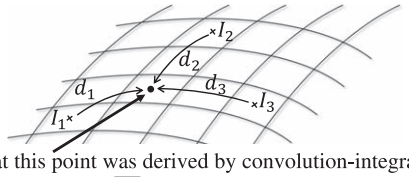

Quantity at this point was derived by convolution-integration as follows:

$$D = \sum_i f(d_i) \times I_i \, , i = 1, 2, 3, \ldots$$

I_i : Number of neutrons terminated in mesh i
d_i : Distance from center of mesh i
$f(d_i)$: Kernel value at d_i away from center of mesh i

Figure 2. Overview of convolution-integration in the hybrid algorithm. The values I_i in mesh i constitute the distribution of neutrons terminated below the cut-off energy and are multiplied by the values f of the point-kernel at a distance d_i from mesh i. The products for mesh i are used to derive quantity D at each point.

was isotropic. Details of the kernel calculation are presented in section 2.1.2.

Second, an MC calculation with a cutoff function for neutrons was performed to derive the in-phantom distribution of neutrons terminated below 1 eV. In addition, the distributions of the boron dose, nitrogen dose, and number of secondary gamma-rays produced in the phantom, arising from the reaction of neutrons with energy of >1 eV, were derived. However, the contributions were expected to be small because these doses are mainly produced by the reactions of thermal neutrons. Furthermore, the fast neutron dose attributed to ^{1}H(n, n)^{1}H and the dose attributed to primary gamma-ray mixing in the neutron irradiation field were determined.

Third, the in-phantom distribution of the neutrons terminated with energy of ⩽1 eV was convolution-integrated with the kernel, to derive the distributions of the thermal neutron flux, boron dose, nitrogen dose, and number of secondary gamma-ray productions. An overview of the convolution-integration is presented in figure 2. The distribution of neutrons terminated with energy of ⩽1 eV, which constituted the values I, was convolution-integrated with the values f of the kernel represented as a function of the distance d from the source, and the quantity D (thermal neutron flux, boron dose, etc) was derived at each point. Finally, the distribution of the secondary gamma-ray dose was calculated by setting the distribution of the number of gamma-rays produced as the source.

2.1.2. Calculation of kernels

The kernels were calculated in a spherical geometry, with a point source having an energy spectrum of neutrons terminated below the cut-off energy of 1 eV at the center.

The energy spectra of the terminated neutrons on the central axis of each phantom were calculated using the [T-Time] tally function implemented in PHITS. In PHITS, if the energy cutoff is set as 1 eV, the tracking is terminated when the energy of particles is below 1 eV after scattering. In the [T-Time] tally, the particle decelerate below 1 eV after scattering is tallied, and the energy after the scattering is recorded.

The spectra were obtained at the depths between 0 and 6.5 cm with a calculation mesh of 5 mm, and the calculation results were averaged to derive the neutron spectrum. As described in section 3.1, the spectrum did not change significantly with respect to the depth.

Then, using the source spectrum, the kernels for the thermal neutron flux, boron dose, nitrogen dose, and secondary gamma-ray production were derived using PHITS as a function of the distance with a 1-mm mesh.

In addition, kernels were prepared for each calculation associated with the cubic and head phantoms. As shown in figure 1(a), the kernels were calculated in the geometry filled with water or brain tissue.

2.2. Experimental verification using cubic phantom

A cubic phantom filled with boric acid-water was used for the experimental verification of the calculation accuracy for the thermal neutron flux. As shown in figure 3, the volume of the phantom was 20 × 20 × 20 cm^3. The concentration of boron-10 in the boric acid-water was 23 ppm, which is close to the typical concentration of normal tissues in clinical situations (Koivunoro *et al* 2015, Kawabata *et al* 2021) [16, 17]. The thermal neutron fluxes were measured using the gold activation method as follows. A set of bare gold wires (The Nilaco Corporation) with a diameter of 0.25 mm was placed along the central axis and the off-axis direction of the phantom. Gold wires covered with cadmium tubes with a wall thickness of 0.5 mm were used to remove the contribution of the thermal neutron component from the activation reaction. The bare and cadmium-covered gold wires were irradiated by an epithermal neutron beam (CO-0000F mode) at the Heavy Water Neutron Irradiation Facility of Kyoto University Reactor (KUR-HWNIF) (Sakurai *et al* 2002) [18]. This neutron irradiation was operated with the power of 1 MW. (In the clinical trial, the irradiation had been operated with the power of 5 MW, and the order of thermal neutron flux had been 10^9 n (cm^2·s)$^{-1}$). The irradiation field was formed using a

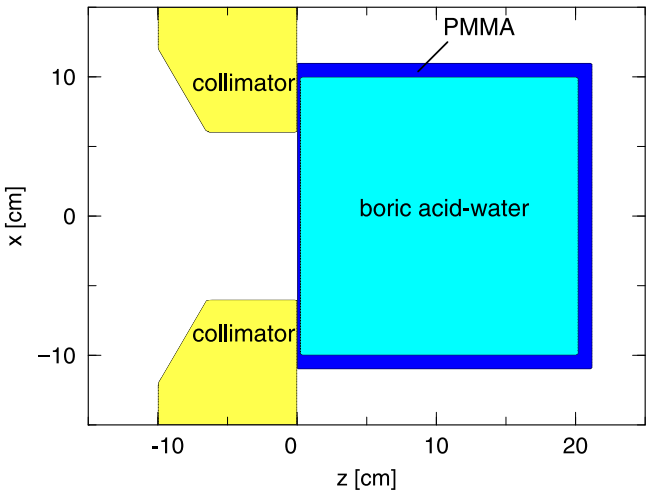

Figure 3. Horizontal cross-sections of the geometry in the experimental verification using the cubic phantom at KUR-HWNIF with the reactor power of 1 MW [18].

polyethylene collimator containing LiF with an aperture diameter of 12 cm. After irradiation, the activated gold wires were cut into small pieces with lengths of 5 mm or 1 cm, and 412-keV gamma-rays emitted from the activated gold wire at each point of the phantom were measured using an NaI(Tl) scintillation detector (SP-20, Ohyo Koken Kogyo Co., Ltd). Subsequently, the rates of the ^{197}Au(n, γ)^{198}Au reaction of the bare and cadmium-covered gold wires were derived from the number of emitted gamma-rays, and the thermal neutron fluxes were determined from the difference between the reaction rates of the bare and cadmium-covered gold wires (ASTM E262-17, 2017) [19].

In addition, the thermal neutron flux distributions in the geometry simulating the experiment were obtained by the 'entire-full-MC' calculation using only the full-energy MC method and the 'entire-hybrid' calculation using only the hybrid algorithm. The kernel used in the 'entire-hybrid' calculation was calculated in a spherical geometry with a radius of 30 cm, filled with boric acid-water with a ^{10}B concentration of 23 ppm. In the MC calculation of the in-phantom distribution for both of the 'entire-full-MC' and 'entire-hybrid' calculations, a mesh size of $5 \times 5 \times 5$ mm^3 was used. The calculation results were compared with the results obtained via the aforementioned measurement.

2.3. Calculations using complementary approach for humanoid phantom simulating head region

2.3.1. Complementary approach adopting full-energy MC method for shallow region alone

In the 'complementary' calculation, the entire region was separated into two regions at the boundary, which were a few centimeters from the body surface of the head phantom, to prevent the overestimation of the thermal neutron flux near the beam incident surface of the phantom. Hereinafter, the inward distance perpendicular to the body surface is called the 'separation depth'. The separation depth was set as 4 cm in this study. In addition, the region from the body surface to the separation surface is called the 'shallow' region, and the region within the separation surface is called the 'deep' region.

In the 'complementary' calculation, the convolution in Step 2 shown in figure 1(a) was performed to derive the distribution only in deep region, and the full-energy MC calculation was performed for shallow region, as shown in figure 1(b). In Step 1, an MC calculation with a cut-off function for the neutrons was performed to derive the in-phantom distribution of neutrons terminated with energy of $\leqslant$1 eV. In addition, the distributions of the boron and nitrogen doses attributed to the reactions of neutrons with energies of $>$1 eV were derived for the deep region. Furthermore, the fast neutron dose, primary gamma-ray dose, and secondary gamma-ray dose attributed to the reactions of neutrons with energies of $>$1 eV were determined for the entire region. Note that fast neutron dose distribution was obtained via MC calculation using the cut-off function for the entire region, and the separation depth was not set in the calculation. This is because the contribution of neutrons below a cut-off energy of 1 eV was considered sufficiently small to be neglected. In Step 2, the region was separated into shallow and deep regions. In Step 2-1, the in-phantom distribution of the neutrons terminated with energy $\leqslant$1 eV was convolution-integrated with the kernels to derive the distributions of the thermal neutron fluxes, boron dose, nitrogen dose, and number of secondary gamma-rays produced in the phantom for the deep

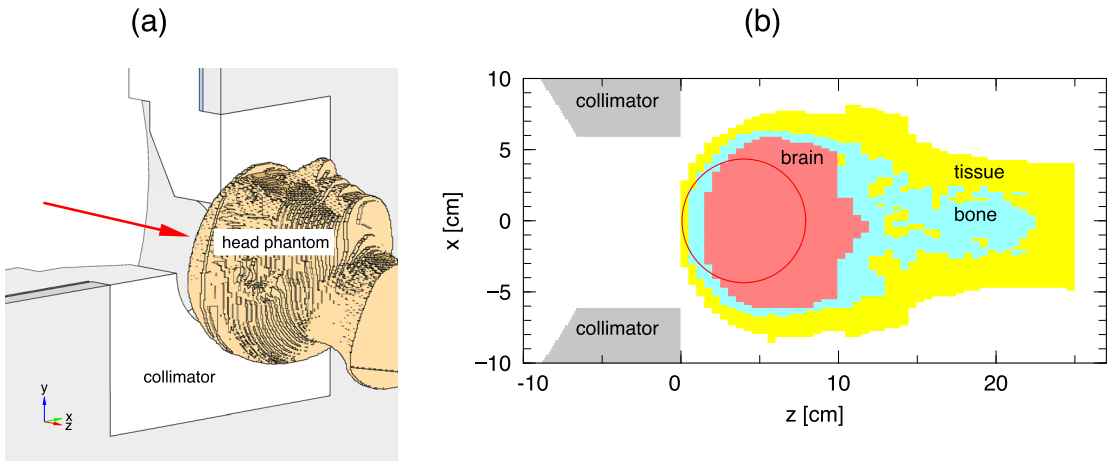

Figure 4. (a) Three-dimensional view and (b) coronal cross-section of geometry simulating a humanoid head. An epithermal neutron beam is irradiated from the top of the head through the aperture of the collimator, as indicated by the red arrow in (a). The red circle in (b) shows the reference region for the statistical uncertainty evaluation.

region. In Step 2–2, full-energy MC calculations were performed to obtain the aforementioned doses for the shallow region. In Step 3, the distribution of the secondary gamma-ray dose generated by the neutron capture reactions with ^{1}H, ^{10}B, ^{40}Ca, and ^{31}P peresent in the phantom and collimator was derived using the MC calculation with only photon transport. In this step, the distributions of the number of secondary gamma-ray productions calculated in step 2 were used as the gamma-ray source.

2.3.2. Dose calculation using humanoid phantom simulating head region

The geometry of the humanoid phantom simulating the head region used for calculations is shown in figure 4. An epithermal neutron beam was simulated to be irradiated from the top of the head through the aperture of the collimator at the KUR-HWNIF. A voxel phantom was constructed from computed tomography images of the phantom, and soft tissues, brain, and cranial bones were assigned to each voxel with a boron-10 concentration of 25 ppm [16, 17]. The elemental composition and density of each material were obtained from National Institute of Standards and Technology and International Committee for Radiological Units Report 46 [20, 21]. In addition, the kernel used for the 'complementary' calculation was calculated in a spherical geometry with a radius of 30 cm filled with brain tissues with a boron-10 concentration of 25 ppm [16, 17].

Furthermore, doses administered to a normal brain by neutron irradiation to the top of the head, assuming the treatment for brain tumours, were determined using the following equations:

$$\text{Boron dose} = CBE \times D_{\text{B}} \quad (1)$$

$$\text{Nitrogen dose} = RBE_{\text{N}} \times D_{\text{N}} \quad (2)$$

$$\text{Fast neutron dose} = RBE_{\text{F}} \times D_{\text{F}} \quad (3)$$

$$\text{Gamma-ray dose} = RBE_{\text{G}} \times D_{\text{G}} \quad (4)$$

Here, D_{B}, D_{N}, D_{F}, and D_{G} represents the physical boron, nitrogen, fast neutron, and gamma-ray doses, respectively. D_{B} was calculated by setting the boron-10 concentration as 25 ppm [16, 17]. D_{N} and D_{F} were calculated by setting the concentrations of nitrogen and hydrogen as 2.0 wt% and 11.1 wt%, respectively (Sakurai *et al* 2002) [18]. D_{B} was weighted by a compound biological effectiveness (CBE) value of 1.35 (Kawabata *et al* 2008) [22]. D_{N} and D_{F} were weighted by a relative biological effectiveness (RBE) value of 3.0, and D_{G} was weighted by an RBE value of 1.0 (Kawabata *et al* 2008) [22]. The total dose was calculated as the sum of those RBE- or CBE-weighted doses.

In this study, the dose distributions and computation time were evaluated according to the doses administered to a normal brain as presented in the previous paragraph. Note that the dose distribution in other materials, such as tissue, bone, and tumor, can be obtained by the scaling according to such parameters as the concentration of elements, RBE, CBE. in each material because each of the boron, nitrogen, and gamma-ray production dose kernels were prepared as values per density of elemental (1 wt% or ppm).

2.3.3. Evaluation of computation time and accuracy

For the 'complementary' calculation, the computation time was evaluated as the total time required only for the MC calculations because the time required for the convolution-integration was considered negligible. The computation times in Steps 1, 2–2, and 3 of the 'complementary' calculation were defined as T_1, T_2, and T_3, respectively, as shown in figure 1. Each of the times T_1, T_2, and T_3 was estimated as the computation time required to achieve the desired statistical uncertainty of $<$1% of each dose relative to the total dose for all dose components. This condition is expressed as follows:

$$\left(\frac{u_B}{D_T} < 0.01\right) \wedge \left(\frac{u_N}{D_T} < 0.01\right) \wedge \left(\frac{u_F}{D_T} < 0.01\right) \wedge \left(\frac{u_G}{D_T} < 0.01\right) \quad (5)$$

Here, the symbol '∧' denotes a logical conjunction. In addition, $u_{B/N/F/G}$ was defined as the uncertainty of each RBE or CBE-weighted dose, which was derived from each statistical uncertainty of the boron, nitrogen, fast neutron, and gamma-ray doses, and D_T was defined as the total dose. This condition maintained the uncertainty of the total dose at <2%, which satisfies the recommendation of the American Association of Physicists in Medicine Report 13 for the uncertainty of dose computation [23]. The reference region for the statistical uncertainty evaluation was defined within a spherical volume with a 4-cm radius centered at a 4-cm depth on the beam axis, as indicated by the red circle in figure 4(b), according to the conditions used by Kumada *et al* [10]. The time required for the 'entire-full-MC' calculation was estimated as the time required for satisfying equation (5) in the region.

To evaluate the calculation accuracy, each dose distribution obtained via the 'complementary' calculation for the determined times was compared with that obtained via the 'entire-full-MC' calculation. Here, the MC calculations included in both the 'entire-full-MC' and 'complementary' calculations were conducted with a mesh size of 5 × 5 × 5 mm^3. Additionally, in the 'complementary' calculation, the distributions of the thermal neutron fluxes were calculated for both the shallow and deep regions. Each dose distribution calculated using the hybrid algorithm for the deep region was normalized to match the thermal neutron flux calculated by adopting the hybrid algorithm for the deep region to the value calculated by adopting the full-energy MC method for the shallow region at the separation depth on the central axis.

2.4. Calculation of each dose component using PHITS

The calculations using PHITS were performed as follows. First, the in-phantom distribution of neutrons terminated below the cut-off energy of 1 eV was calculated using the [T-Time] tally.

In addition, the thermal neutron flux was calculated using the [T-Track] tally. The boron, nitrogen, and fast neutron doses were calculated using the [T-Track] tally with the multiplier subsection, as follows:

$$D = \int \{K(E) \times \phi(E) \times w\}\, dE, \quad (6)$$

where D, $K(E)$, and w represent the physical dose, kerma coefficient, and mass fraction of elements in a compound (water, tissue, brain tissue, or bone), respectively. The elements associated with the boron, nitrogen, and fast neutron doses are ^{10}B, ^{14}N, and ^{1}H, respectively. Moreover, E represents the neutron energy, and $\phi(E)$ represents the neutron flux.

The gamma-ray doses were calculated using the [T-Deposit] tally, for which the kerma approximation was adopted.

In the 'entire-full-MC' calculation that has been normally used, the gamma-ray doses were directly calculated via the simultaneous transport calculation of neutrons and gamma-rays. In contrast, in the calculation using the hybrid algorithm, the distribution of the number of secondary gamma-ray productions was set as the gamma-ray source, as described at the end of section 2.3.1 and in figure 1. Then, the gamma-ray dose was determined via the transport calcuation for only gamma-rays.

The number of secondary gamma-ray productions R_G was calculated using the [T-Track] tally with the multiplier subsection using the following equation:

$$R_G = \int \{\sigma(E) \times \phi(E) \times N\}\, dE, \quad (7)$$

where $\sigma(E)$ represents the gamma-ray production cross-section of ^{1}H, ^{10}B, ^{40}Ca, or ^{31}P, and N represents the number density of each ^{1}H, ^{10}B, ^{40}Ca, and ^{31}P nucleus in each compound.

3. Results

3.1. Prepared kernel for hybrid algorithm

Figure 5(a) shows the neutron source spectra used for kernel calculation. As described in section 2.1.2, in the [T-Time] tally that was used to calculate the spectrum, the particle decelerated below 1 eV after scattering is tallied, and the energy after the scattering is recorded. Therefore, the range of the energy spectrum was 0 to 1 eV. These neutron source spectra were derived by averaging the spectra at depths of 0.25 to 6.25 cm, and the spectra were similar for all depths. In addition, the averaged neutron spectra did not depend on the shapes of the cubic and head phantoms, as shown in figure 5(a). However, this was not sufficiently verified. Therefore, in this study, each spectrum was used for the calculation of the distribution in each geometry. Figure 5(b) shows the kernel used for the calculation of thermal neutron fluxes in the head region, as an example.

3.2. Comparison of calculations with experiment using cubic phantom

To validate the calculation accuracy of the hybrid algorithm, the thermal neutron flux distribution obtained via the 'entire-hybrid' calculation, using only the hybrid algorithm, was compared with the measured distribution in the phantom. In addition, the results obtained via the 'entire-full-MC' calculation using only the full-energy MC method were compared with the measured data to confirm the calculation accuracy of the full-energy MC method. Figure 6 shows the in-phantom distributions of the thermal neutron flux along the central axis and off-axis

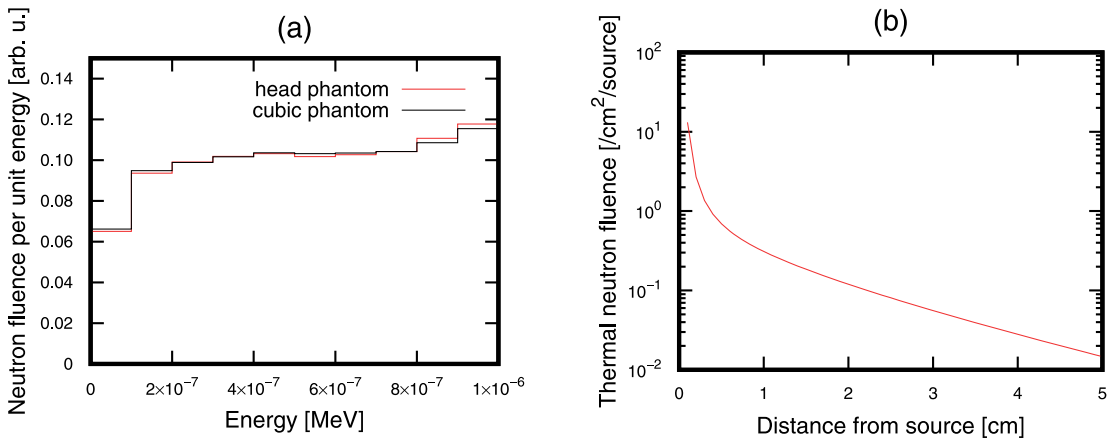

Figure 5. (a) Neutron source energy spectra used for calculating the kernel and (b) an example of the kernel used for deriving the thermal neutron flux for the hybrid algorithm.

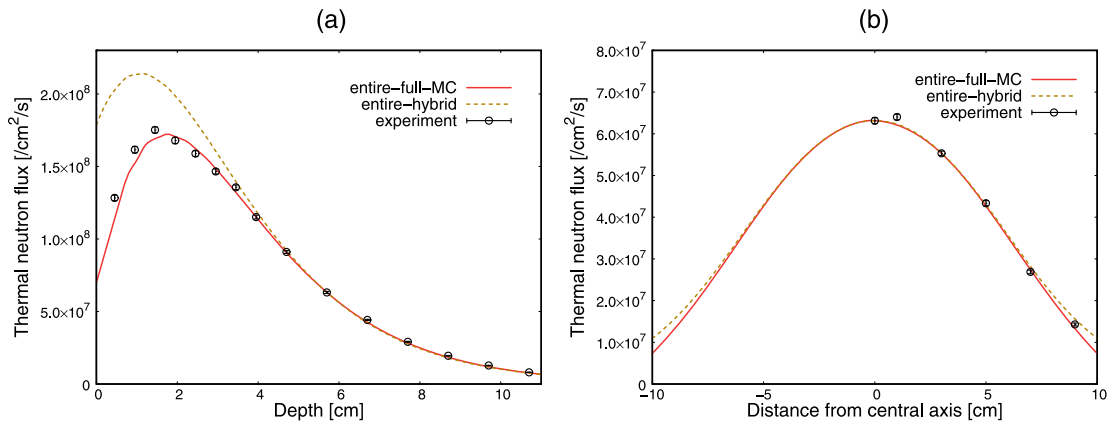

Figure 6. (a) Depth and (b) off-axis distributions of the thermal neutron flux in the cubic phantom; (b) shows the thermal neutron fluxes at the points of 5.7 cm from the incident surface of the cubic phantom. Neutron irradiation was performed with the reactor power of 1 MW.

direction. Here, the calculated distributions were normalized to match the flux with the measured value at the depth of 5.7 cm. As shown in figure 6(a), the depth distribution obtained via the 'entire-hybrid' calculation reproduced the measured distribution at depths of $\geqslant$4 cm and overestimated it at depths of $<$4 cm. The 'entire-hybrid' calculation overestimated the measurement by 20% at the peak position of the measured distribution at a depth of 1.45 cm, and the maximum difference from the 'entire-full-MC' calculation was 156% at the surface. In addition, the peak position in the result obtained via the 'entire-hybrid' calculation was shifted to a shallower depth compared with the measurement result. At all depths, the results obtained via the 'entire-full-MC' calculation agreed well with the measurement results.

Furthermore, as shown in figure 6(b), the off-axis values obtained via the 'entire-hybrid' calculation exceeded the measured values near the side surface of the phantom, whereas those obtained via the 'entire-full-MC' calculation agreed well with the measured values from side to side.

3.3. Comparison with calculation using full-energy MC method for humanoid head phantom

The 'complementary' calculation using the full-energy MC method and the hybrid algorithm was compared with the 'entire-full-MC' calculation, using only the full-energy MC method, with regard to the computation time and accuracy.

Table 1 presents the computation times needed to achieve the condition that the statistical uncertainty of each dose relative to the total dose was less than 1% for all dose components. The required total times were 52 min for the 'complementary' calculation and 86 min for the 'entire full-MC' calculation. The 'entire-hybrid' calculation was not performed for the head region; however, the computation time was expected to be 39 min excluding the full-energy MC calculation for the shallow region. Furthermore, the

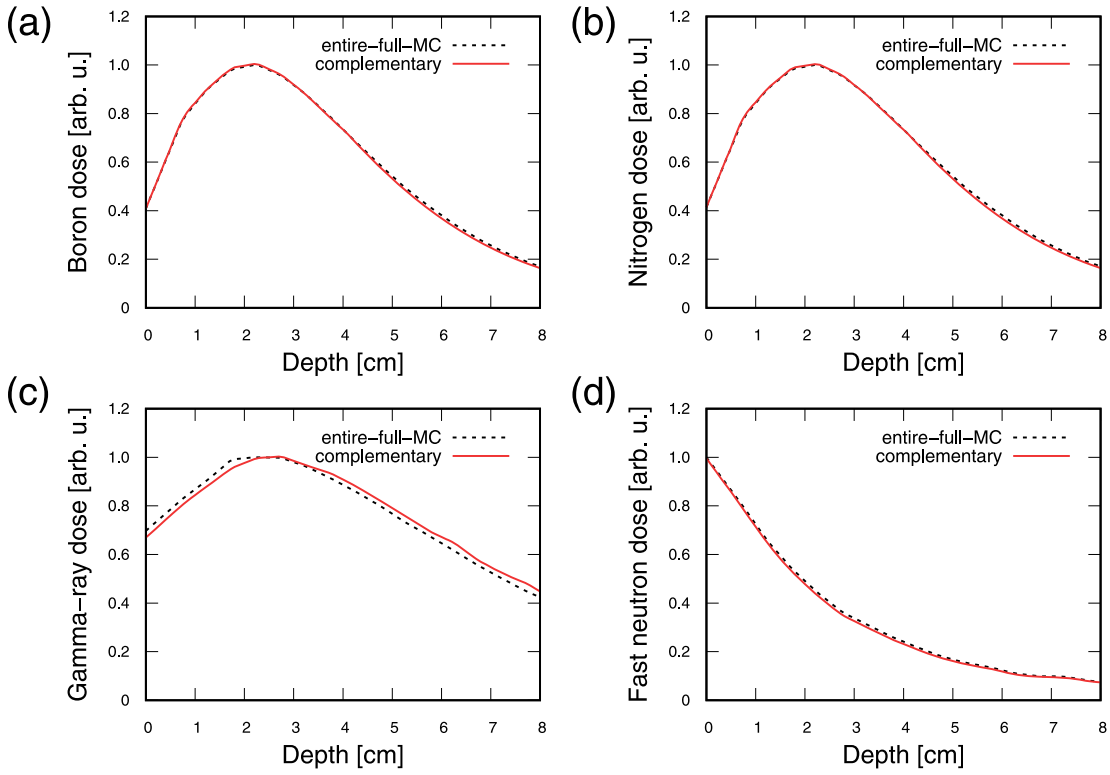

Figure 7. Depth distributions of the (a) boron, (b) nitrogen, (c) gamma-ray, and (d) fast neutron doses obtained calculating for the time shown in table 1. Black dotted lines indicate the results of the 'entire-full-MC' calculation, and red lines indicate the results of the 'complementary' calculation. The boron and nitrogen dose distributions in the shallow region were calculated using only the full-energy MC method, and the results agreed well with the 'entire-full-MC' calculation results.

time required for the MC calculation with a cut-off function was mostly determined by the time required for the calculation of the fast neutron dose, and the calculation of the fast neutron dose took longer to converge than those of the other doses.

In the hybrid algorithm, modeling the thermalization process as a kernel is essential; therefore, the time required to calculate the boron dose was estimated to confirm the effect of the modeling on reducing the computation time. Table 2 presents the computation time required to achieve a relative statistical uncertainty of $<1\%$ for a boron dose. The required total computation times were 25 min for the 'complementary' calculation and 41 min for the 'entire-full-MC' calculation. In addition, the time required for the MC calculation with the cut-off function was expected to be equal to that required for the 'entire-hybrid' calculation, and it was 2 min.

Figures 7 and 8 show the dose distributions obtained for the computation times presented in table 1. The depth distributions of the boron, nitrogen, fast neutron, and gamma-ray doses obtained via the 'entire-full-MC' and 'complementary' calculations are shown in figure 7. The distributions of the total doses on the central axis and in the coronal cross-section were compared, as shown in figure 8. Here, each maximum value of the results obtained via the 'entire-full-MC' calculation was normalized to 1 on the central axis, and then each result obtained via the 'complementary' calculation was normalized using the normalization factor that was employed for the 'entire-full-MC' calculation.

As shown in figures 7(a) and (b), the distributions of the boron and nitrogen doses obtained via the 'complementary' calculation agreed well with the results obtained via the 'entire-full-MC' calculation. Figure 7(c) shows the distribution of the gamma-ray doses. The doses obtained via the 'complementary' calculation were slightly higher than those obtained via the 'entire-full-MC' calculation for the deep region. Figure 7(d) shows the distributions of the fast neutron doses. The doses obtained via the 'complementary' calculation agreed well with those obtained via the 'entire-full-MC' calculation.

Figure 8(a) shows the depth distributions of the total dose. The distributions obtained via the 'complementary' calculation agreed well with the results obtained via the 'entire-full-MC' calculation for all depths. The maximum difference between the results of the 'complementary' and 'entire-full-MC' calculations was small ($<2\%$). Figures 8(b) and (c) show the distributions in the coronal cross-section and the distribution of the difference from the result obtained via the 'entire-full-MC' calculation. The distributions obtained via the 'complementary' calculation agreed well with the results obtained via the 'entire-full-MC' calculation.

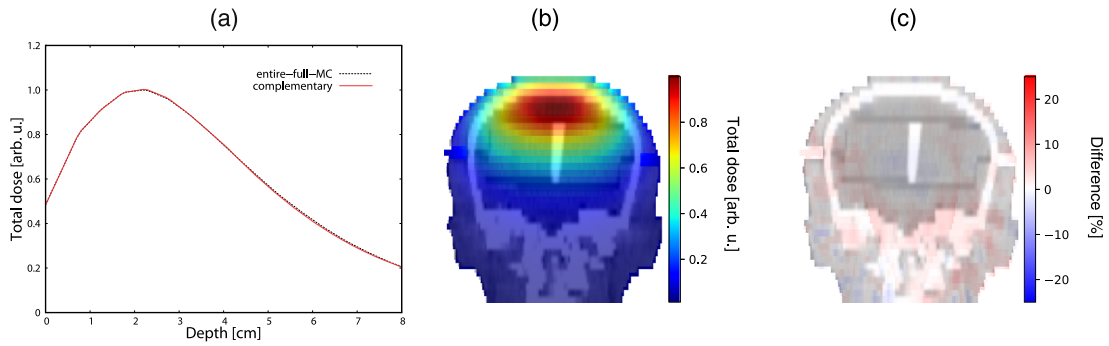

Figure 8. Total dose distributions and the difference between results obtained via the 'complementary' and 'entire-full-MC' calculations: (a) depth distribution on the central axis; (b), (c) distribution and the distribution of the difference in the coronal cross-section.

Table 1. Time [min] required for the calculation of all doses.

Calculation contents	'complementary' calculation	'entire-full-MC' calculation
MC calculation with cut-off function for neutron	38	—
Full-energy MC calculation for shallow region	13	86
Photon transport calculation	1	—
Total calculation	52	86

Table 2. Time [min] required for calculation of the boron dose.

Calculation contents	'complementary' calculation	'entire-full-MC' calculation
MC calculation with cut-off function for neutrons for deep region	2	—
Full-energy MC calculation for shallow region	23	41
Total calculation	25	41

4. Discussion

In the experimental verification, the calculation accuracy of the hybrid algorithm was verified by comparing the 'entire-hybrid' calculation result with the measurement result in terms of the thermal neutron flux distribution. The 'entire-hybrid' calculation partially reproduced the measured values at depths of >4 cm. However, it overestimated the results in the shallower region. In contrast, the 'entire-full-MC' calculation accurately reproduced the measurement results. As described in 4th paragraph in the Introduction section, the overestimation by the 'entire-hybrid' calculation was caused by neglecting the leakage of neutrons from the phantom to the surrounding air in the kernel calculation.

Considering the overestimation of the thermal neutron flux in the shallow region by the hybrid algorithm, the 'complementary' calculation was tested. The 'complementary' calculation was compared with the 'entire-full-MC' calculation for a geometry simulating the head region. For the boron and nitrogen doses, which were proportional to the thermal neutron fluxes, the maximum difference between the results obtained via the 'entire-full-MC' and 'complementary' calculations was 5%. The 'entire-hybrid' calculation overestimated the thermal neutron fluxes in a cubic phantom by 156% compared with the 'entire-full-MC' calculation near the surface, as described in section 3.2. Therefore, the complementary calculation was confirmed to be more accurate in calculations related to thermal neutron compared to the calculation using only the hybrid algorithm.

In addition, the calculation accuracy of the complementary approach was evaluated with regard to the fast neutron and gamma-ray doses for the geometry simulating the head region. The distributions of the fast neutron dose obtained via the 'complementary' calculation agreed well with those obtained via the 'entire-full-MC' calculation. This was attributed to the small contribution of neutrons with energies of $\leqslant 1$ eV to the fast neutron dose. The distributions of the gamma-ray doses obtained via the 'complementary' calculation had slightly higher values than those obtained via the 'entire-full-MC' calculation for the deep region. This was attributed to the slight overestimation of the number of secondary gamma-ray productions in the deep region.

Furthermore, the calculation accuracy of the depth distribution of the total dose was high in the

depth range of 0–8 cm on the central axis. With regard to the distribution in the coronal cross-section, the 'complementary' calculation accurately reproduced the 'entire-full-MC' calculation result.

The time required for the 'complementary' calculation was reduced by approximately 40% relative to that for the 'entire-full-MC' calculation. If the 'entire-hybrid' calculation is performed for the head region, the computation time could be reduced by 55% relative to the 'entire-full-MC' calculation. Because a cut-off function could be employed for the neutron transport in the MC calculation used in the 'complementary' calculation, the time required for a single neutron transport was reduced by approximately half, and the total computation time was reduced.

Here, setting the separation depth as 4 cm was attributed to the experimental verification. The depth distribution obtained via the 'entire-hybrid' calculation reproduced the measured distribution at depths $\geqslant$4 cm. This indicated that using a separation depth of 4 cm allows high calculation accuracy in the deep region, where the hybrid algorithm is applied, with the minimum calculation time consumed in the MC calculation in the shallow region.

Additionally, we estimated the impact in the case of changing the separation depth by conducting the calculation using the separation depth of 3 cm. Compared with that for separation depth of 4 cm, the total computation time was reduced by only 2 min, and the calculation accuracy became lower because the hybrid algorithm was applied to the shallower side.

In the calculation using the separation depth of $>$4 cm, the computation time would be longer because the full-energy MC method was applied to the deeper region, and the calculation accuracy would not significantly change because the maximum difference between the depth distributions derived by the 'complementary' approach using the separation depth of 4 cm and 'entire-full-MC' calculations was below 2% and sufficiently small. Therefore, the optimal separation depth is considered to be 4 cm from the balance of the accuracy.

The time required for the calculation of the fast neutron dose accounted for most of the total time required for the MC calculations in both the 'entire-full-MC' and 'complementary' calculations. In the MC calculation, the convergence of the statistical uncertainty of the fast neutron dose was the slowest among all the doses—particularly in the deep region where few particles could maintain high energy. Accordingly, the total computation time was dominated by the time needed to calculate the fast neutron dose, which was reduced by using the cut-off function, as described in the 5th paragraph in this section.

However, we considered that modeling the thermalization process of the neutrons as a kernel in the hybrid algorithm can reduce the time required for dose calculation. The time required for the 'entire-hybrid' calculation only for the boron dose was expected to be 2 min, which was equal to the time required for the MC calculation with the cut-off function, as shown in table 2. In contrast, the time required for the 'entire-full-MC' calculation was 41 min. The boron dose is dominant for BNCT and is mostly attributed to the thermalization process which is modeled in the hybrid algorithm. In the calculation of the distribution attributed to the thermalization process, the hybrid algorithm can reduce the computation time by 95% compared to the full-energy MC method. Therefore, modeling the thermalization process of the neutrons can reduce the time required for dose calculation.

The calculation accuracy of the hybrid algorithm was high for the calculation in the deep region, as shown by the results such as figure 6. Therefore, the hybrid algorithm can reduce the computation time, while maintaining high calculation accuracy in the calculation of the distribution attributed to the thermalization process for the deep region.

5. Conclusion

In this study, a newly developed hybrid algorithm was explored, and its calculation accuracy was verified. Subsequently, a complementary approach using both the hybrid algorithm and full-energy MC method was applied, and the computation time and calculation accuracy were verified. In the experimental verification, the calculation using the hybrid algorithm reproduced the measurement result at depths $\geqslant$4 cm and overestimated it at depths $<$4 cm. This was attributed to the currently adopted kernel being calculated in a homogeneous geometry with a large volume. Thus, in the dose calculation using a geometry simulating the head region, the full-energy MC method was adopted in the shallow region from the phantom surface to the separation surface, which was a few centimeters from the body surface of the head phantom, and the hybrid algorithm was adopted in the deep region inside the separation surface with the optimal separation depth of 4 cm. This complementary calculation required a shorter time than the calculation using the full-energy MC method for the entire region, while maintaining nearly the same accuracy. The calculation results for only the boron dose attributed to the thermal neutron showed that the hybrid algorithm significantly reduced the computation time compared with the full-energy MC method. Therefore, we conclude that the modeling of the thermalization process of neutrons as a kernel in the hybrid algorithm reduces the time required for dose calculation in BNCT.

Acknowledgments

We would like to thank Editage (www.editage.com) for English language editing. We are grateful to Dr

Ryota Iwasaki for generously providing us with knowledge about pharmacokinetics of boron compounds.

Data availability statement

All data that support the findings of this study are included within the article (and any supplementary files).

Funding

This work was supported by JSPS KAKENHI (Grant Number JP20K08078).

ORCID iDs

Takushi Takata https://orcid.org/0000-0001-6436-6130
Naonori Hu https://orcid.org/0000-0003-2702-3344
Hiroki Tanaka https://orcid.org/0000-0002-6195-3177

References

[1] Locher G L 1936 Biological effects and therapeutic possibilities of neutron *Am. J. Roentgenol.* **36** 1–13
[2] Barth R F *et al* 2012 Current status of boron neutron capture therapy of high grade gliomas and recurrent head and neck cancer *Radiat. Oncol.* **7** 1–21
[3] Fairchild R G and Goodman L J 1965 Development and dosimetry of an 'epithermal' neutron beam for possible use in neutron capture therapy i. 'epithermal' neutron beam development *Phys. Med. Biol.* **11** 491–504
[4] Suzuki M 2020 Boron neutron capture therapy (BNCT): a unique role in radiotherapy with a view to entering the accelerator-based BNCT era *Int. J. Clin. Oncol.* **25** 43–50
[5] Tanaka H *et al* 2009 Characteristics comparison between a cyclotron-based neutron source and KUR-HWNIF for boron neutron capture therapy *Nucl. Instrum. Methods Phys. Res. B* **267** 1970–77
[6] Kato T *et al* 2020 Design and construction of an accelerator-based boron neutron capture therapy (AB-BNCT) facility with multiple treatment rooms at the Southern Tohoku BNCT Research Center *Appl. Radiat. and Isot.* **156** 1–9
[7] Kanno H *et al* 2021 Designation products: boron neutron capture therapy for head and neck carcinoma *The Oncologist* **26** e1250–5
[8] Sumitomo Heavy Industries, Ltd, World's first BNCT systems as medical device (https://shi.co.jp/english/info/2019/6kgpsq0000002ji0.html)
[9] Hu N *et al* 2021 Evaluation of a treatment planning system developed for clinical boron neutron capture therapy and validation against an independent Monte Carlo dose calculation system *Radiat. Oncol.* **16** 243
[10] Kumada H *et al* 2018 Development of a multimodal monte carlo based treatment planning system *Radiat. Prot. Dosimetry* **180** 286–90
[11] Sato T *et al* 2018 Features of particle and heavy ion transport code system (PHITS) version 3.02 *J. Nucl. Sci. Technol.* **55** 684–90
[12] Takada K *et al* 2016 Development of Monte Carlo based real-time treatment planning system with fast calculation algorithm for boron neutron capture therapy *Phys. Med.* **32** 1846–51
[13] Albertson B J, Blue T E and Niemkiewicz J 2001 An investigation on the use of removal-diffusion theory for BNCT treatment planning: a method for determining proper removal-diffusion parameters *Med. Phys.* **28** 1898–904
[14] Ahnesjö A, Andreo P and Brahme A 1987 Calculation and application of point spread functions for treatment planning with high energy photon beams *Acta Oncol.* **26** 49–56
[15] Nojiri M *et al* 2022 Verification of complementary approach using full-energy Monte Carlo method and partial kernel-based method for fast dose calculation in BNCT *Jpn. J. Med. Phys. Suppl.* 1 **42** 112
[16] Koivunoro H *et al* 2015 Biokinetic analysis of tissue boron (^{10}B) concentrations of glioma patients treated with BNCT in Finland *Appl. Radiat. Isot.* **106** 189–94
[17] Kawabata S *et al* 2021 Accelerator-based BNCT for patients with recurrent glioblastoma: a multicenter phase II study *Neurooncol Adv.* **3** 1–9
[18] Sakurai Y and Kobayashi T 2002 The medical-irradiation characteristics for neutron capture therapy at the heavy water neutron irradiation facility of kyoto university research reactor *Med. Phys.* **29** 2328–37
[19] ASTM E262-17 2017 *Standard Test Method for Determining Thermal Neutron Reaction Rates and Thermal Neutron Fluence Rates by Radioactivation Techniques.* (West Conshohocken, PA: ASTM International)
[20] National Institute of Standards and Technology, X-Ray Mass Attenuation Coefficients, table 2. Material constants and composition assumed in the present evaluations for compounds and mixtures. (https://physics.nist.gov/PhysRefData/XrayMassCoef/tab2.html) (13 January 2022, data last accessed)
[21] White D R, Griffith R V and Wilson I J 1992 Appendix A: body tissue compositions. In: ICRU Report 46: photon, electron, proton and neutron interaction data for body tissues *Journal of the ICRU* **os-24** 11–13
[22] Kawabata S *et al* 2008 Boron neutron capture therapy for newly diagnosed glioblastoma *J. Radiat. Res.* **50** 51–60
[23] American Association of Physicists in Medicine 1984 *Report No. 13: Physical aspects of quality assurance in radiation therapy* (New York: American Institute of Physics) (https://doi.org/10.37206/12)